JMEPEG (2017) 26:1513–1530
DOI: 10.1007/s11665-017-2547-4

1059-9495/$19.00

Microstructures, Forming Limit and Failure Analyses of Inconel 718 Sheets for Fabrication of Aerospace Components

K. Sajun Prasad, Sushanta Kumar Panda, Sujoy Kumar Kar, Mainak Sen, S.V.S. Naryana Murty, and Sharad Chandra Sharma

(Submitted August 11, 2016; in revised form November 17, 2016; published online February 27, 2017)

Recently, aerospace industries have shown increasing interest in forming limits of Inconel 718 sheet metals, which can be utilised in designing tools and selection of process parameters for successful fabrication of components. In the present work, stress-strain response with failure strains was evaluated by uniaxial tensile tests in different orientations, and two-stage work-hardening behavior was observed. In spite of highly preferred texture, tensile properties showed minor variations in different orientations due to the random distribution of nanoprecipitates. The forming limit strains were evaluated by deforming specimens in seven different strain paths using limiting dome height (LDH) test facility. Mostly, the specimens failed without prior indication of localized necking. Thus, fracture forming limit diagram (FFLD) was evaluated, and bending correction was imposed due to the use of sub-size hemispherical punch. The failure strains of FFLD were converted into major-minor stress space (σ-FFLD) and effective plastic strain-stress triaxiality space (ηEPS-FFLD) as failure criteria to avoid the strain path dependence. Moreover, FE model was developed, and the LDH, strain distribution and failure location were predicted successfully using above-mentioned failure criteria with two stages of work hardening. Fractographs were correlated with the fracture behavior and formability of sheet metal.

Keywords electron microscopy, finite element modeling, fractography, fracture forming limit diagram, Inconel 718, limiting dome height

1. Introduction

Inconel 718 (IN718) is a precipitation-hardenable nickel-chromium-iron-based superalloy extensively used for aerospace applications such as fuel tanks, heat exchangers and several engine components under cryogenic (−250 °C) to elevated temperature conditions (705 °C) (Ref 1-3). Recently, IN718 sheets are found to be suitable for manufacturing of gas bottles to store high-pressure oxygen for space missions (Ref 4). Also, this alloy is used in outer casings of nickel-hydrogen (Ni-H_2) cells to store energy for the satellite power systems (Ref 5). IN718 possesses high fatigue resistance to sustain pressure variations during the charging and discharging cycles of the Ni-H_2 cell. Also, this material is compatible with alkali (KOH) and offers strong resistance to hydrogen embrittlement under operational environment. Apart from the high strength, its ductility is very high due to continuous strain-hardening ability of this complex alloy system during uniaxial deformation (Ref 6). Hence, the above-mentioned lightweight casings can be stamped by the critical design of press tools and process parameters.

The conventional strain-based forming limit diagram (FLD) of various automotive grade steel, aluminum and magnesium alloy sheets had been successfully evaluated in the past, and moreover, these were implemented as a diagnostic tool for failure prediction during stamping (Ref 7-14). The detailed procedure of evaluation of FLDs was discussed by Keeler (Ref 15), Goodwin (Ref 16) and Hecker (Ref 17). It was found that very limited attention had been paid in the past on extensive investigations of cold-forming behavior of IN718 thin sheet metal. There is previous literature available for readers on the constitutive behavior of this material incorporating both strain hardening and thermal softening at elevated temperature and strain rate under uniaxial deformation mode (Ref 18-20). In order to obtain precise component with better surface finish, the aerospace industries preferred solution-treated IN718 materials while stamping under room temperature. Moreover, the strength of the component further increased due to strain hardening at room temperature deformation. In the context of room temperature formability, Roamer et al. (Ref 6) evaluated the limiting strains of three different nickel-based superalloys including that of IN718 sheet material of 0.5 mm thickness. The FLDs were plotted without localized necking data during tension-tension deformation mode due to rapid propagation of fracture. This onset of fracture without a hint of localized necking in IN718 material was due to the presence of a large number of second-phase particles.

Recently, fracture forming limit diagram (FFLD) was used to predict failure of sheet materials where fracture/tearing was observed without visible necking. In this context, several researchers measured the fracture strains in the thickness direction and the surface fracture strains were estimated considering failure to be under plane strain deformation mode

K. Sajun Prasad and **Sushanta Kumar Panda**, Department of Mechanical Engineering, I.I.T. Kharagpur, Kharagpur, WB 721302, India; **Sujoy Kumar Kar** and **Mainak Sen**, Department of Metallurgical and Materials Engineering, I.I.T. Kharagpur, Kharagpur, WB 721302, India; and **S.V.S. Naryana Murty** and **Sharad Chandra Sharma**, VSSC, Indian Space Research Organisation, Thiruvananthapuram, Kerala 695022, India. Contact e-mail: sushanta.panda@mech.iitkgp.ernet.in.

(Ref 21-29). There was no open literature available on FFLD of IN718 materials, and hence, for readers' understanding a brief background in this regard is mentioned. The evaluation of FFLD was of immense interest in incremental sheet metal forming processes (Ref 26), where the failure was reported in the form of splitting without the onset of prior necking. Embury and Duncan (Ref 27) first reported similar kind of observations in equi-biaxial tensile deformation of Al alloys (6061 and 2036-T4), where the formability limits by necking and fracture interacted in such a way that the fracture of the sheet took place without prior localized necking. It was reported that the FFLDs of aluminum and steel sheets were linear shape showing higher ductility limit, and the shape was well characterized as per ductile failure criteria (Ref 28). However, Jain et al. (Ref 29) reported the shape of FFLD of AA6111 sheets touching the FLD near the equi-biaxial strain path. The shape and failure limit strains of automotive grade sheets depend on the type of failure mode resulting from the void nucleation, growth and coalescence from the presence of inclusions, precipitates, hard second-phase particles, etc., and also from the activation of shearing instabilities. Hence, there were no general failure criteria to predict the complete shape of the FFLD for different ferrous and non-ferrous sheet metals. It is necessary to deform IN718 sheet materials under multiple stages progressively to fabricate gas bottles and Ni-H_2 cell casings having higher depth compared to its diameter. The forming limit of this material is very important while designing the tools and process sequence to obtain a defect-free component.

Despite the wide usage and benefits of strain-based FLD and FFLD, it was found that the limiting strains were strongly influenced by strain path during multistage deformation to get the desired three-dimensional complex shapes (Ref 30-33). An alternative solution is converting limiting strains into stress space to get the stress-based forming limit diagrams (σ-FLDs) and stress-based fracture forming limit diagrams (σ-FFLDs). Also, recently, researchers have reported that the hydrostatic stress and stress triaxiality influenced fracture mechanism in metals (Ref 34-36).

From the above discussion, we understand that it is extremely important to evaluate the formability of IN718 sheet material for the successful fabrication of gas bottles and Ni-H_2 cell casings without failure of the components. It is noteworthy that the sheet materials may undergo complex strain paths while imparting the desired shape during the sheet forming process. Therefore, the main objectives of the current research work are: (a) to evaluate the failure limiting strains by deforming the IN718 sheet materials under different strain states using laboratory scale LDH tests, (b) to estimate the failure limit into stress space and effective plastic strain (EPS)-stress triaxiality $(\bar{\varepsilon}, \eta)$ space that aerospace industries can use as a diagnostic tools for failure prediction while fabricating sheet metal components, (c) to understand the microstructure and failure mechanism during the deformation and (d) to validate the estimated failure limits by FE modeling of the LDH tests that considers Hill-48 plasticity theory and double-stage hardening behavior observed from the tensile test of IN718

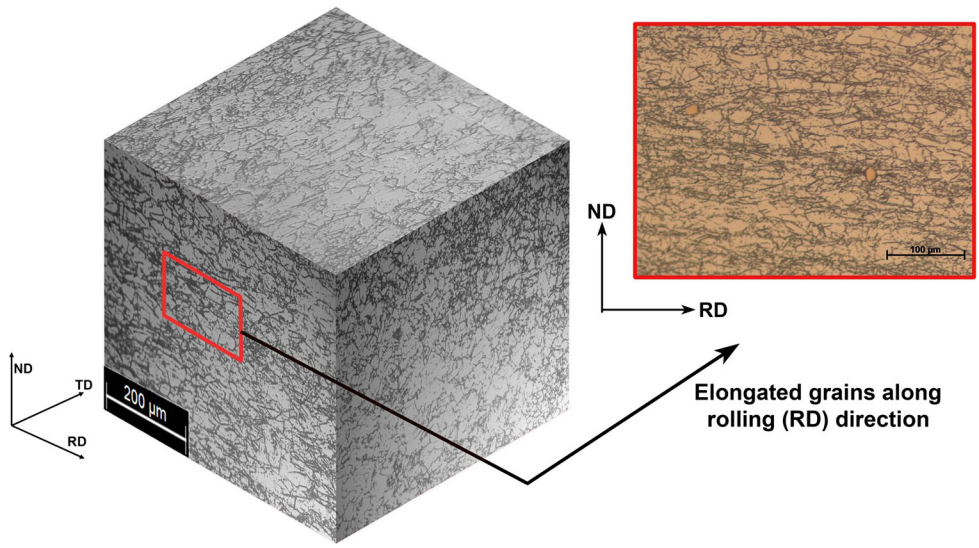

Fig. 1 Optical microstructure of IN718 used in the present study in three planes with right inset revealing the elongated grains in ND-RD plane

Table 1 Chemical composition of IN718 used in the present study (wt.%)

Element	Ni	Cr	Fe	Nb	Mo	Ti	Al
wt.%	52.93	18.01	18.80	5.25	2.95	1.06	0.69
Element	**S**	**Mn**	**Cu**	**C**	**Si**	**Co**	
wt.%	0.01	0.07	0.07	0.05	0.10	0.01	

material. The coefficient of friction was estimated and incorporated in the FE model to predict and validate deformation behavior with the experimental data successfully.

2. Materials and Methods

2.1 IN718 Composition and Microstructure

A batch of mill-annealed IN718 material sheets of 1.2 mm thickness (AMS specifications 5596 Ref 37) was selected in the present study. Figure 1 shows the microstructure obtained by light microscopy, showing an average grain size of 14 μm with a difference in morphology in rolling (RD), transverse (TD) and normal (ND) directions. Mostly compressed and elongated grain structure can be observed in the ND-RD plane (right inset of Fig. 1), which can be attributed to large-scale rolling to obtain the sheet material. However, equiaxed compressed grains are observed in the ND-TD plane. The chemical composition evaluated by x-ray fluorescence (XRF) analysis is shown in Table 1. As reflected from Table 1, IN718 is one of the most intricate alloy systems with compositional complexity. Hence, different kinds of strengthening precipitates are expected as reported in the earlier literature (Ref 2, 38). A major amount of Ni (52.93%) signifies the substantial contribution of strength from solid solution strengthening, which may occur due to the higher solubility of many added alloying elements such as Fe, Cr and Mo. The addition of Cr and Al is very useful for improving oxidation resistance on the surface of the material through the oxide formation of corresponding elements. Additions of Cr, Mo, Al, Nb and Ti not only provide solid solution strengthening but are also the basis for precipitation hardening. Hence, in order to identify different precipitates in the material which contribute to strengthening, scanning electron microscopy (SEM), electron backscatter diffraction (EBSD) and high-resolution transmission electron microscopy (HRTEM) were carried out. The samples were electrically etched/polished using a mixture of oxalic acid and water in the ratio of 1:10 for SEM and EBSD analysis. Also, the electron transparent samples (ϕ3 mm) were prepared by ion milling to observe microstructures at high magnification in HRTEM.

2.2 Tensile Test

Flat tensile specimens were fabricated from the mill-annealed IN718 sheets by wire-cut electrical discharge machining process as per ASTM-E8M standard (Ref 39), and the schematic drawing is depicted in Fig. 2. Specimens were cut along three orientations with respect to the rolling direction (RD) of the sheets, viz., parallel (0°), diagonal (45°) and perpendicular (90°) directions. The tensile tests were conducted in a 100-kN servo-hydraulic universal testing machine at a crosshead speed of 2 mm/min. The tensile response in terms of true stress-strain was estimated from the engineering stress-strain data obtained from the machine. Also, the different tensile properties such as 0.2% yield strength (YS), ultimate tensile strength (UTS), total elongation, strength coefficient (K), strain-hardening exponent (n), normal anisotropy coefficient ($\bar{r}$) and planar anisotropy coefficient (Δr) were evaluated. The n and K values of the material were quantified using Hollomon (Ref 40) and Swift hardening (Ref 41) law as per Eq 1 and 2.

$$\bar{\sigma} = K\bar{\varepsilon}^{n} \quad \text{(Eq 1)}$$

$$\bar{\sigma} = K(\varepsilon_0 + \bar{\varepsilon})^{n} \quad \text{(Eq 2)}$$

The Lankford anisotropy coefficients (r values), which signifies resistance to thinning and further facilitates the material flow into the die cavity, were evaluated in three directions with respect to RD (viz., r_0, r_{45} and r_{90}) (Ref 3). Also, the jump test at room temperature was conducted to evaluate the strain rate sensitivity index (m) of the material using the technique developed by Backofen et al. (Ref 42).

2.3 Limiting Dome Height Test

Laboratory scale LDH setup comprising of the sub-size hemispherical punch of ϕ50 mm was used to conduct out-of-plane stretch forming experiments to save material. The

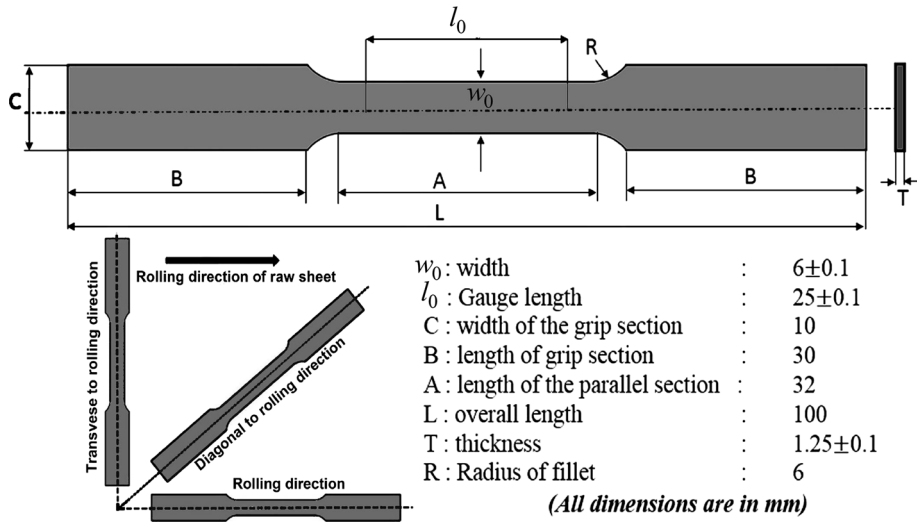

Fig. 2 Schematic of the standard ASTM-E8M tensile specimen with three differently oriented samples (0°, 45°, and 90°) with respect to the rolling direction of the sheet

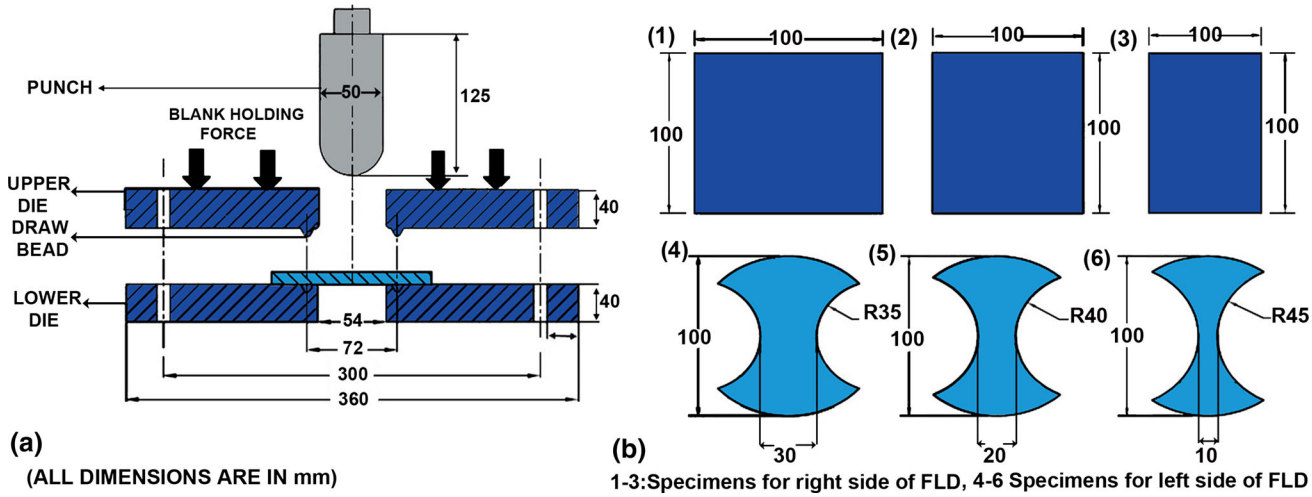

Fig. 3 Schematic displaying: (a) LDH test setup with a punch and die assembly and (b) specimen geometry (rectangular and Hasek specimens)

schematic diagram of the setup with the upper and lower dies is shown in Fig. 3(a), and all the tools were mounted in a 100-ton double-action hydraulic press. The hydraulic press was integrated with a load cell and LVDT to capture the load-displacement data during the testing. The dies had an internal draw bead designed to avoid the flow of flange material into the cavity during the forming test. IN718 sheet metals of different geometry as shown in Fig. 3(b) were cut, and these were deformed by the rigid punch after clamping in between the dies. A mirror was placed below the lower die to observe the appearance of necking/failure during the test. Also, a drop in load was observed during failure of the samples. The 100 mm × 100 mm square shape specimens were used to induce biaxial tensile strain in the material, and sufficient lubrication using polyethylene sheet with hydraulic oil was used as a lubricant to impose deformation close to equi-biaxial strain path. Rectangular specimens of the same length but the narrower width of 80 and 60 mm were deformed to change the strain path during deformation. However, failure in the sheet metals was consistently observed at the draw-bead position during the testing of rectangular specimens of 40 mm width. Hence, the Hasek specimen geometries as shown in Fig. 3(b) were used. In these specimens, the material could flow into the die cavity from the lateral side as the width was lower than the draw-bead diameter. However, the sheet metal gets locked in draw bead and stretched in the longitudinal direction. The quantity of material drawing into the die cavity depended on the width of the specimen, and this induced the compressive strain and hence the strain path. Circular grids of 2.5 mm diameter were etched electrochemically on the surface of IN718 sheet metal before deformation to measure the maximum safe and necked/failure surface strains. The circular grids turned into ellipses after deformation, and both the major and minor diameters were measured using Leica stereo zoom microscope. The major (e_1) and minor (e_2) engineering strains were evaluated by Eq 3 and 4, and further, these were transformed into corresponding true strains ($\varepsilon_{1,2m}$) as per Eq 5. The major and minor strain data obtained from the safe and failed regions were plotted in strain locus. To confirm the accuracy, four specimens were tested in each condition repeatedly.

$$e_1 = \frac{(\text{Ellipse major axis distance} - \text{grid diameter})}{(\text{Ellipse major axis distance})} = \frac{(d_1 - d_0)}{d_1} \quad \text{(Eq 3)}$$

$$e_2 = \frac{(\text{Ellipse minor axis distance} - \text{grid diameter})}{(\text{Ellipse minor axis distance})} = \frac{(d_2 - d_0)}{d_2} \quad \text{(Eq 4)}$$

$$\varepsilon_{1,2m} = \ln(1 + e_{1,2}) \quad \text{(Eq 5)}$$

It was of particular interest that a sub-size hemispherical punch of ϕ50 mm was used in the present work instead of the standard punch of ϕ101.4 mm as proposed by Hecker (Ref 17). Hence, the bending strain induced on the outer surface of the sheet metal while wrapped around the smaller punch during deformation was calculated using Eq 6. The strain gradient along the thickness of sheet due to bending was extensively reported in the previous literature (Ref 43-46). It can be observed from Eq 6 that the bending strain increases with a decrease in the radius of curvature. Further, the measured surface strains ($\varepsilon_{1,2m}$) were combinations of stretching and bending strains. The onset of necking and subsequent failure in the sheet metal occurred due to thinning induced from pure stretching. In order to correct the failure surface strain, the calculated bending strains were deducted from the measured surface strains using Eq 7 in all the samples deformed in different strain paths.

$$\varepsilon_{\text{bending}} = \ln\left(1 + \frac{t_f}{2R_n}\right) \quad \text{(Eq 6)}$$

$$\varepsilon_{1,2} = \varepsilon_{1,2m} - \varepsilon_{\text{bending}} \quad \text{(Eq 7)}$$

where $t_f = t_0 \exp(-\varepsilon_{1m} - \varepsilon_{2m})$, ε_{1m} and ε_{2m} represent measured true major and minor surface strains, t_0 = initial thickness, t_f = instantaneous thickness (onset of necking) and R_n = radius of curvature of the middle surface of the sheet.

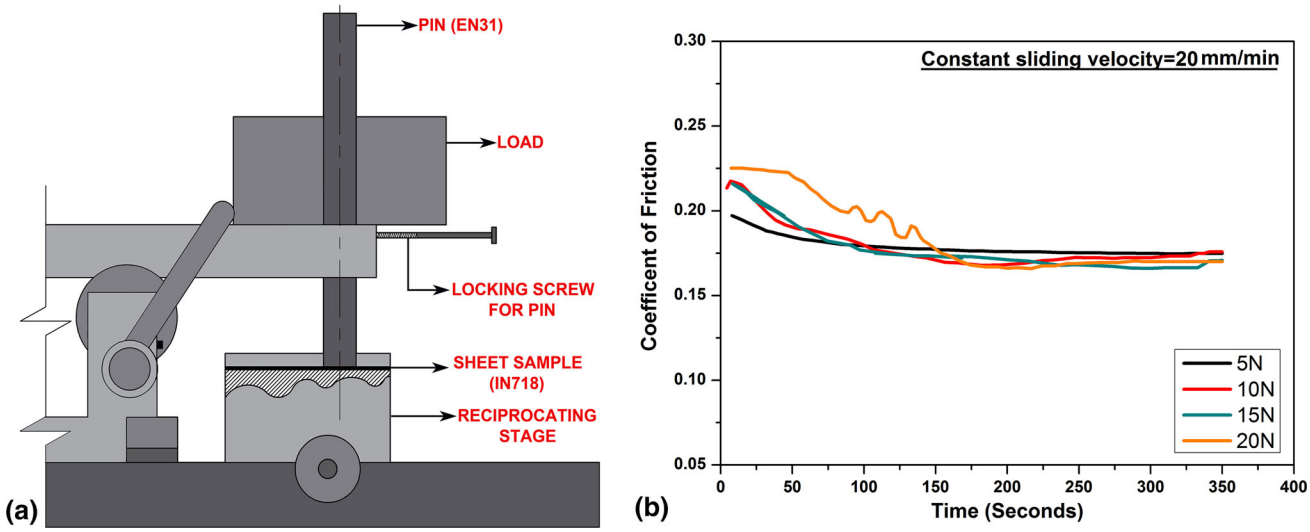

Fig. 4 Friction test: (a) schematic of test setup and (b) variation of measured coefficient of friction at different loading conditions at a constant sliding velocity of 20 mm/min

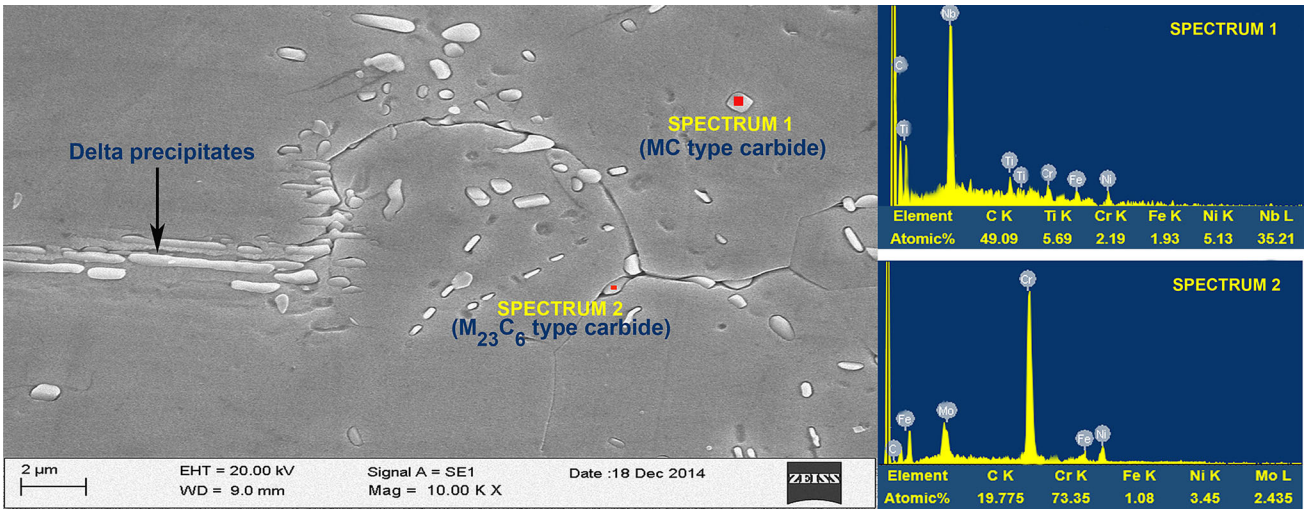

Fig. 5 SEM image showing the carbides and δ precipitates in the IN718 material used in the present study

2.4 Friction Test

In sheet forming processes, the formability, strain distribution and strain path during deformation are significantly influenced by the friction and lubrication at the sheet-tool interface. Moreover, the coefficient of friction is required to be incorporated in the FE models. Hence, the coefficient of friction (COF) was evaluated by a flat pin of ϕ10 mm and 100 mm length. The pin made of EN31 material was mounted on a stiff lever and further loaded onto the IN718 sheet metal in a linear reciprocating mode in a CSM Tribometer as shown in Fig. 4(a). The relative sliding velocity of the pin on the sheet sample was kept at a constant velocity of 20 mm/min to maintain the exact quasi-static deformation condition of the current forming process. The tribological tests were performed under different normal load conditions such as 5, 10, 15 and 20 N, respectively, with a test run of 350 s in an environment-controlled enclosure protecting from humidity. The COF was continuously recorded during all the tests. It can be observed from the experimentally obtained graphs as shown in Fig. 4(b) that the COF reached a stable state of approximately 0.175. It may be due to the reduction of the asperities level considerably after 150 s regardless of the normal load during the test.

3. Results and Discussion

3.1 Microstructure

3.1.1 SEM Analysis. The SEM micrograph shown in Fig. 5 reveals carbides as well as large δ precipitates. The alloy has a carbon content of 0.047%, and it combined with active elements such as niobium and titanium to form MC-type carbides ($(Ti_{0.11}Cr_{0.06}Fe_{0.03}Ni_{0.10}Nb_{0.70})$ C). These carbides were embedded within the matrix with blocky morphology as reported in the previous literature (Ref 47). Further, the EDS results confirmed the presence of MC carbides as depicted in Fig. 5. These MC carbides decomposed into lower carbides ($M_{23}C_6$ and M_6C) during solution annealing (Ref 48), and

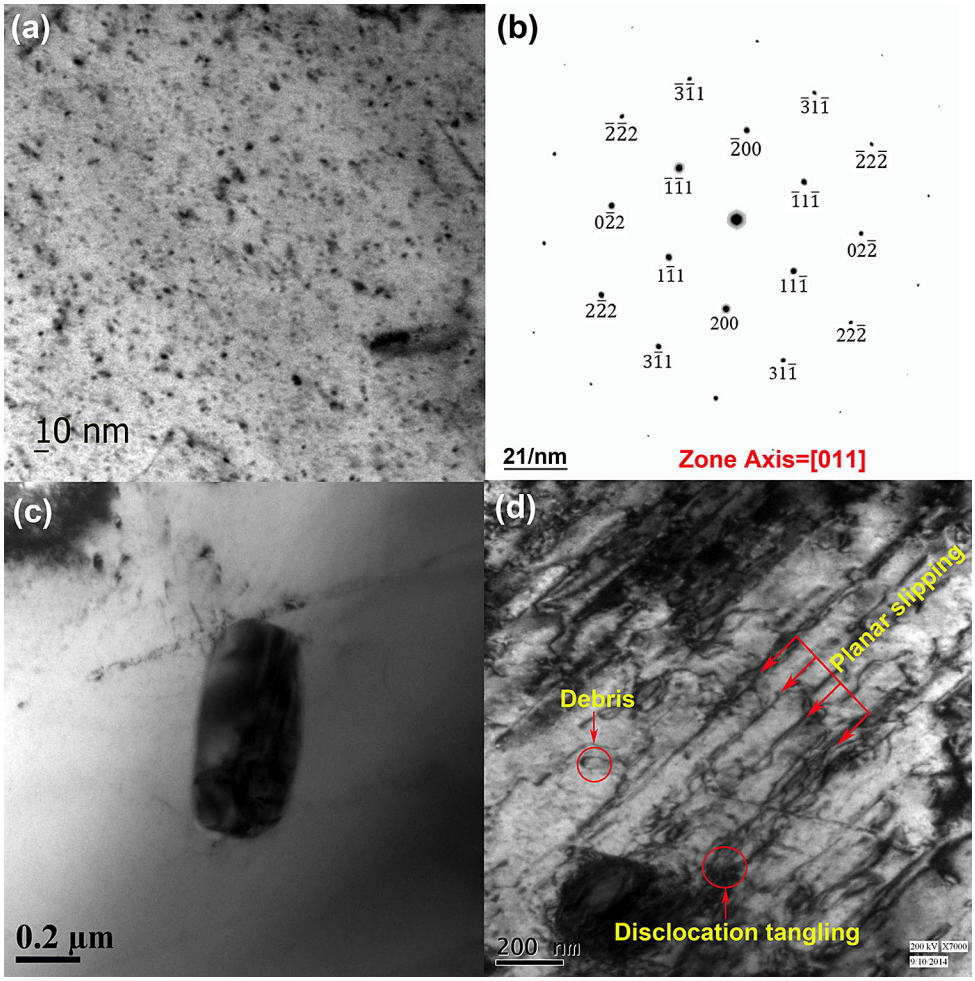

Fig. 6 TEM images showing (a) BF image of nanoprecipitates, (b) corresponding selected area diffraction (SAD) pattern (zone axis <011>), (c) BF image of delta precipitate, (d) dislocation structures indicating planar slipping, dislocation tangling and some debris

traces of $(Cr_{0.92}Fe_{0.01}Ni_{0.04}Mo_{0.03})_{23}C_6$ were found at the grain boundaries from EDS spectrum analysis. This irregularly shaped carbide may offer both oxidation and hot corrosion resistance to the material. Further, the presence of these carbides at the grain boundaries increases the rupture strength at high temperature (Ref 49). There was no trace of M_6C in the material, and this might be due to the low contribution of Si (0.1%) for the formation of this type of structure, which was discussed in earlier studies (Ref 50). Apart from carbides, the δ precipitates of long needle/plate-shaped in the range of 1-3 μm length and width of 0.3 μm were also observed within the matrix. These precipitates might have resulted from the high-solution heat-treatment temperature.

3.1.2 TEM Analysis. The nanoprecipitates (γ'', γ' and δ) and dislocation structures were observed by TEM. Figure 6(a) shows a bright field (BF) image with electron beam parallel to <011> zone axis. The corresponding selected area diffraction (SAD) pattern is shown in Fig. 6(b) with the indexed diffraction spots. The γ'' precipitates observed in the BF image were uniformly distributed in the matrix. These precipitates had ellipsoidal disk morphology with an average major and minor length of approximately 8 and 4 nm respectively. Also, clusters of γ' precipitates of the very fine spherical shape of <4 nm were identified within the matrix.

The as-received IN718 materials had been solutionized by heating to 970 °C for 1 h, and the material was quenched rapidly without subsequent aging heat treatment. Hence, the strengthening γ'' precipitates did not grow, and these precipitates remained in such nanosize in the matrix. Because of the small size of the γ'' precipitates, the superlattice reflections from these precipitates did not show enough intensity. Hence, attempts to image these precipitates in usual dark field imaging mode using the superlattice reflections were unsuccessful. Also, rectangular δ precipitate of approximate length 0.65 μm with a width of 0.35 μm was traced in the matrix by TEM BF image (Fig. 6c). The change in the shape of these precipitates from the needle (Fig. 5) to rectangular (Fig. 6c) shape may have occurred due to the cold rolling of the sheet material (Ref 51). The dislocation structures are shown in Fig. 6(d), and mainly planar arrangement of dislocations along with some tangling and debris can be observed. Due to a lower size (<10 nm) of strengthening precipitates, easy shearing may occur which leads to encouraging ductility of the material.

3.1.3 Texture Analysis. Electron backscatter diffraction (EBSD) study was done to determine the orientation of the Ni grains. EBSD scan was taken in a selected area of 600 μm × 500 μm with a step size of 1.5 μm. Due to the presence of phases like δ and carbides, a small fraction of non-indexed

points were also present in obtained orientation map. EBSD data were analyzed by TSL software. During the analysis of the obtained data, the iterative method of grain dilation cleanup was used. Inverse pole figure (IPF) map generated on the cleanedup image is shown in Fig. 7. Also, the pole figures (PF) of the same are also depicted. From the both IPF and PFs, it can be observed that the material is highly textured with a large number of {110} planes being parallel to the normal direction (ND) of the specimen and, therefore, the highest pole density was observed in and around the central region (ND) of (110) PF. The highest pole density was evidenced by the strong intensity value in the intensity contours shown in Fig. 7. It was also found that clusters of {111} planes aligned along an approximate direction of 28° in the ND-RD plane. Thus, results indicated that the as-rolled sheet material showed preferred texture inside the ductile matrix.

3.2 Tensile Properties

The mechanical properties (YS, UTS, total elongation) and Lankford anisotropy coefficients of IN718 sheets determined from uniaxial tensile tests are shown in Table 2. It can be noticed that the material showed almost similar mechanical properties as compared to other aerospace materials such as IN625 and IN718SPF (Ref 6). The high strength of the material helps in attaining high strain energy absorption during dynamic loading due to charging or discharging cycles of the Ni-H_2 cell. It was observed that the total elongation is slightly higher along transverse direction than that of rolling direction, and similar trend had been reported for aluminum alloys by previous researchers (Ref 52). Although the rolled sheet had a preferred texture (Fig. 7), the mechanical properties obtained from tensile testing did not show much difference in three orientations with respect to rolling direction. It may be due to random distribution of strengthening precipitates as discussed in TEM analysis. Hence, IN718 was considered as nearly planar isotropic with respect to overall mechanical properties. However, the average values were calculated using the formula as mentioned in the table due to the minor variations in the properties along three orientations of testing. The excellent ductility and enhanced mechanical properties attracted manufacturers for fabrication of fatigue resisting thin structures by deep drawing and stretch forming operations. The strain rate sensitivity (m) along rolling direction showed a positive value (0.049) at room temperature, which signified that the material flow stress increased very marginally with increasing strain rate. However, the lower value has indicated that this material is not very much sensitive to strain rate in room temperature.

3.2.1 Work-Hardening Capacity. The work-hardening (WH) capacity measured by the uniaxial tensile test is a primary mechanical property that affects the stretch formability. A very high ultimate strength to yield strength ratio of 1.85 was observed in the present material due to very high WH. It may be due to higher dislocation interaction in the material emanated from the activation of slip systems (FCC matrix) in the interior of smaller grains (14 μm). Hence, a higher n value was observed with simultaneous higher % of uniform elongation of the sheet. Thus, in order to explore the effect of WH capacity, a diagram of WH rate ($\theta = \frac{d\sigma}{d\varepsilon}$) versus plastic stress (i.e., the difference between the flow strength and yield stress) was plotted from the data obtained from tension test along rolling direction as depicted in Fig. 8. The curve shows an initial rapid decrease in slope up to a plastic stress of around 95 MPa, which may be due to the transition from elastic to plastic strain domain. This sudden decrease exhibits the presence of elastic property although yielding has initiated. Further, the WH rate continued to decrease gradually till fracture which might have occurred due to easy shearing of very small size nanoprecipitates (< 10 nm) by dislocations (Ref 53). The difference of slopes indicates the presence of two WH stages. It can be further noticed that the WH does not vary significantly beyond a certain value of applied plastic stress, i.e., approximately 900 MPa. This was denoted by saturation stress (σ_{sat}), which could be found out by extrapolating to $\theta = 0$ as shown in Fig. 8.

The point where the true stress curve intersects the curve of WH rate is referred as the point of instability or the onset of diffused necking. The localized necking was expected to occur when half of true stress was intersecting the WH rate curve (Ref 54). However, there was a sudden failure of the specimen just after diffuse necking without the onset of localized necking during the experiment. The failed tensile specimen shown in Fig. 8 corresponds to the fracture point in the graph. The close sectional view along thickness direction showed the shear fracture and further confirmed that the failure occurred without any hint of localized necking. As the material exhibited two stages of WH, it gave encouragement to study the variation of

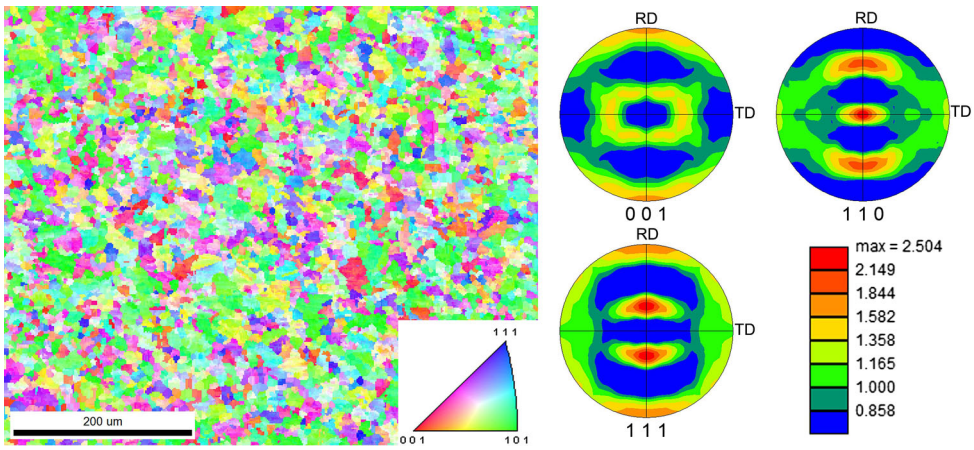

Fig. 7 Inverse pole figure (left) showing the orientation of crystal plane parallel to the normal direction (RD-TD plane) of the sheet metal and pole figure (right) on the RD-TD plane with intensity contours

Table 2 Important mechanical properties obtained from tensile tests in different orientations of the IN718 sheet

Orientation relative to rolling direction	YS, N/mm^2	UTS, N/mm^2	Total elongation, %	Lankford anisotropy parameters, r values	Normal anisotropy, $\bar{r}$	Planar anisotropy, Δr
0°	555 ± 10	1010 ± 10	39.325 ± 0.4	0.781	0.930	−0.030
45°	519 ± 05	973 ± 05	41.525 ± 0.8	0.941		
90°	543 ± 10	991 ± 20	42.253 ± 0.4	1.043		
Avg. (Z)	534 ± 10	986 ± 10	41.157 ± 0.6	…	…	…

$Z = 0.25(Z_0 + 2Z_{45} + Z_{90})$, where Z = YS, UTS, % elongation

$\bar{r} = 0.25(r_0 + 2r_{45} + r_{90})$, $\Delta r = 0.5(r_0 - 2r_{45} + r_{90})$

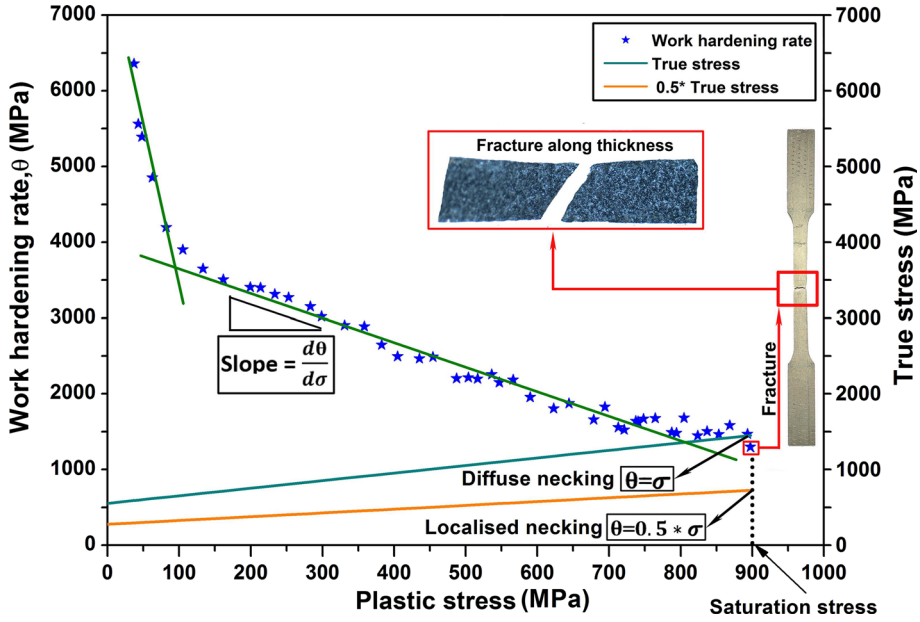

Fig. 8 Work-hardening rate vs. plastic stress in uniaxial tension along rolling direction of the sheet

work-hardening exponent (n value) in all differently oriented specimens using different hardening laws.

3.2.2 Double-Stage Work Hardening. To evaluate the double-stage WH behavior during tensile deformation, a logarithmic plot of true stress versus true strain using Hollomon hardening and Swift hardening laws was used as shown in Fig. 9(a). The trend line on the curve had exhibited double n and K behavior. The validity of trend equation was confirmed by a correlation coefficient of determination (more than 99%). The second-stage n value was significantly higher than that in the first stage, and this increase in n value helped in retaining larger uniform elongation region while deformation. Swift hardening law shows more accurate n value as compared to Hollomon hardening law due to more closeness toward experimental data as observed in all the three orientations with respect to rolling direction. From these observations, it was vital to know the transition of WH stage and the behavior of the material with an increase in plastic strain. From Fig. 9(b), a very high initial WH rate can be observed in the first stage of the WH region (within a plastic strain of 7.5%) in all three orientations. This might be due to the accumulation of dislocation bands, dislocation tangling and splitting of dislocation into partial dislocation on interacting with γ'' particles (Ref 55, 56). A gradual decrease in the second-stage hardening rate with increase in plastic strain (approximately at 0.4) made the material suitable candidate for forming operations. It was observed that the WH rate followed the same trend with very small variation throughout the deformation region in all the three orientations of testing and this was due to the lower planar anisotropy properties.

The formability parameter (Table 2) did not show much difference in three orientations with respect to the rolling direction which affirms the near-isotropic nature of the material. Also, it was found that the material showed relatively lower normal anisotropy (Table 2) as compared to other superalloys such as IN625LCF and IN718SPF (Ref 6), and it might be expected to have poor drawability. However, the weak variations in r value within the plane of sheets (i.e., planar anisotropy) will help in reducing the formation of earing defects in the top edge of the deformed cup-shaped components. The significance of interpreting two-stage hardening behavior, mechanical properties and formability parameters was to implement the deformation behavior in finite element model for better prediction. Moreover, the calibrated FE model will be

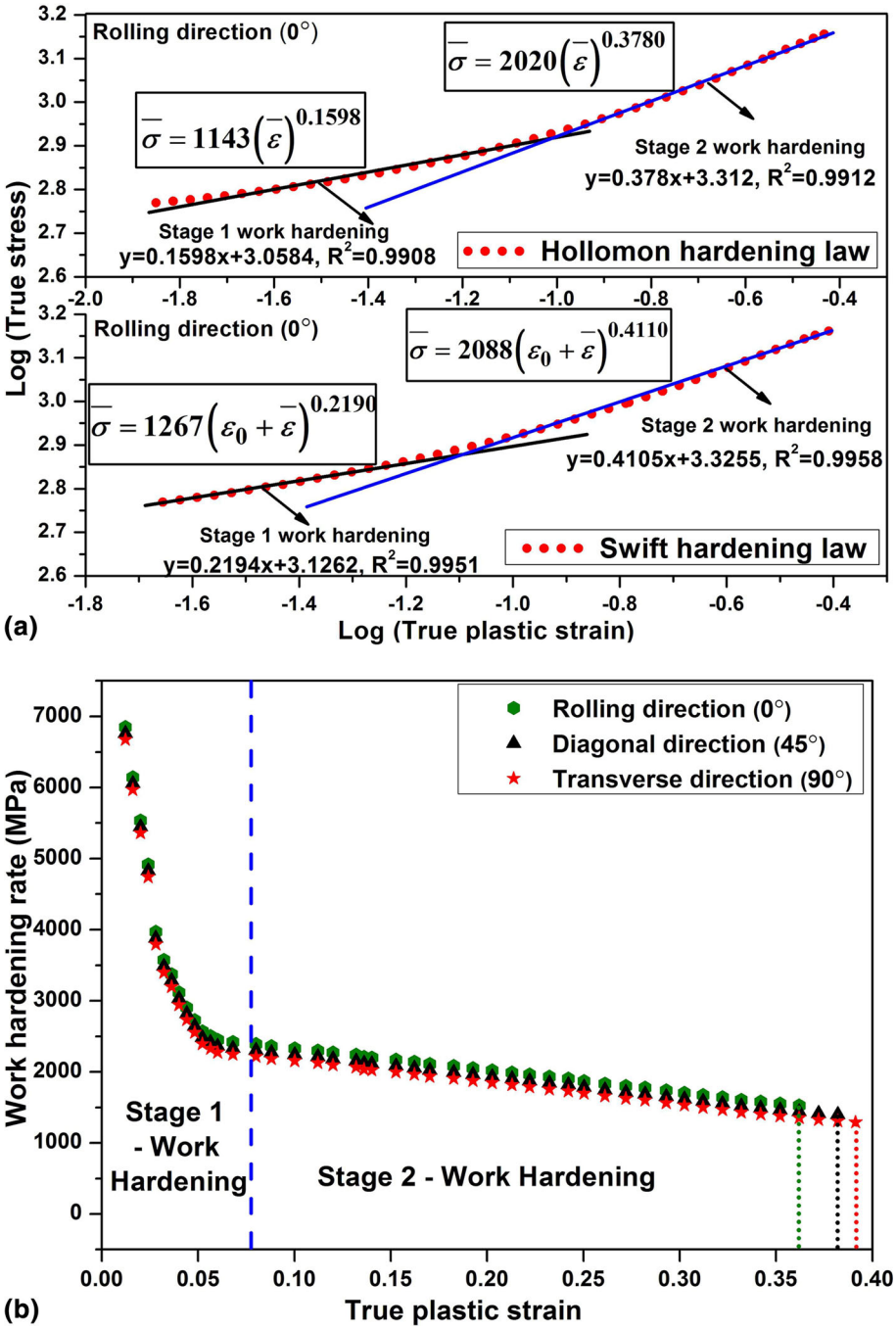

Fig. 9 (a) Logarithmic plot of true stress vs. true plastic strain in rolling direction and (b) work-hardening behavior with increase in plastic strain in all three orientations

used for designing the Ni-H_2 cell and gas bottle casing and in the selection of tool design and process parameters.

3.3 Formability Analysis

3.3.1 Forming Limit Diagram. All the stretch-formed components obtained after the LDH tests are shown in Fig. 10. The major and minor surface strains obtained by measuring the deformed ellipses around the necking/fracture were plotted in strain space to evaluate the forming limit diagram as shown in Fig. 11. Since these strain data were found to be scattered across the whole region, different colors were assigned to distinguish between fractured, necked and safe ellipses. It was evident from the figure that very few numbers of necked ellipses were present in the cluster of fractured grids, and it was due to the failure of sheet metals without the onset of necking during the LDH tests. Hence, the demarcation of limiting strains to plot the forming limit diagram (FLD) was done by drawing a curve separating the maximum safe ellipses from failed ellipses. A very high limiting strain with true major and minor strains of 0.38 and 0.18 was observed in the tension-compression region of FLD, and the strain path during deformation of this ellipse was near to uniaxial tensile deformation mode. The material possessed a lower limiting

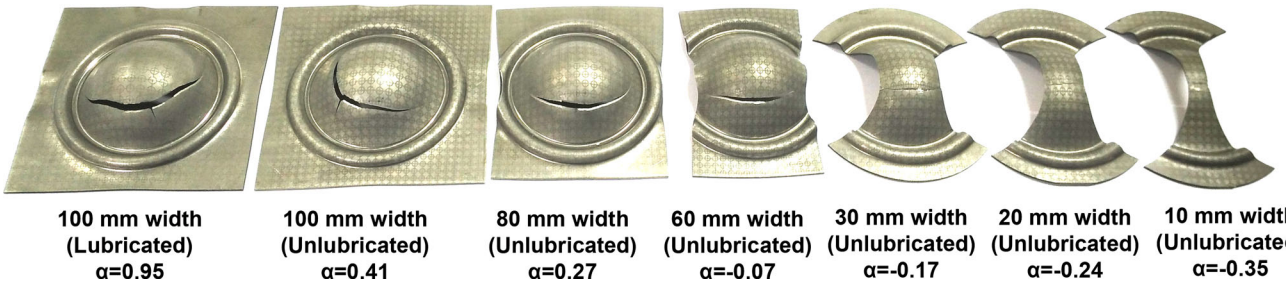

Fig. 10 Fractured LDH test specimens for evaluation of formability limit of IN718

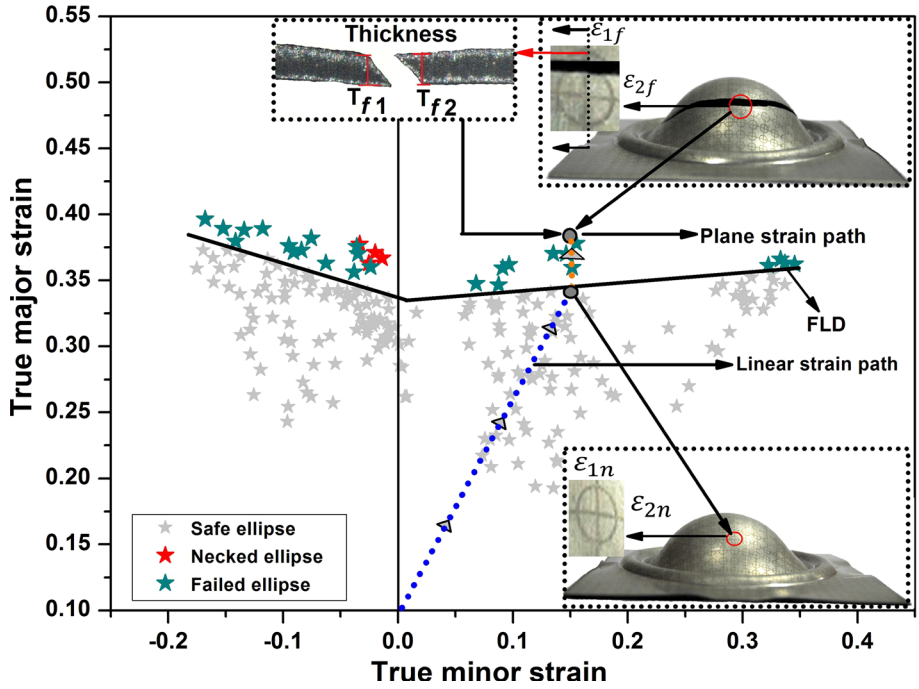

Fig. 11 Forming limit diagram and a typical strain path in biaxial tension region during the deformation of sheet metal up to fracture

strain near to plane strain deformation, i.e., at the intersection point of FLD with true major strain axis (designated as FLD_0), which was often used as a measure of formability.

The FLD_0 of this material was corresponding to a true major strain of approximately 0.34, and it was sufficiently comparable to that of superalloys IN625LCF and IN718SPF (Ref 6). The extreme right-hand side of the FLD was obtained from the LDH testing with a lubricated condition which induced equi-biaxial tension. There was a marginal increase in the limiting major strain to about 0.36 (with a minor strain of 0.35) as compared to the left-hand side of FLD. In the present LDH tests, the through-thickness shear fracture appeared without a visible hint of localized necking as shown in Fig. 11. This observation motivated for further consideration of the formability limits by fracture forming limit diagram (FFLD) as per the discussion in the previous literature (Ref 57). The cyan-colored star symbols in Fig. 10 represented the already fractured ellipses on the surface of the deformed specimens, and these strains did not represent the onset of fracture in the material. In this context, the accurate measurement of surface strains at the onset of fracture during the LDH test was very important.

3.3.2 Fracture Forming Limit Diagram. As it can be observed from Fig. 11, the dotted blue line depicts the linear strain path in tension-tension mode during the deformation of a rectangular specimen in LDH testing till the maximum safe limit. At this current state, the stretched cup had corresponding major (ε_{1n}) and minor (ε_{2n}) surface strains indicating maximum safe limit without any failure inside the ellipse. The stretched cup failed on further deformation, and this resulted in the surface major and minor strains to change to ε_{1f} and ε_{2f}, respectively. It is very well established that the fracture propagates in a plane strain deformation mode, i.e., $\varepsilon_{2n} = \varepsilon_{2f}$ as shown in Fig. 11. The through-thickness section from the dome specimens was cut across the fractured surface, and these were further polished for better visibility under an optical microscope. The perpendicular distance from the start of fracture edge representing the maximum thinned section of the leaf portions was measured (i.e., t_{f1} and t_{f2} as shown in the inset of Fig. 11). The smallest among the two thickness values was considered for evaluating the true thickness fracture strains (i.e., ε_{3f}). Assuming the volume constancy condition during plastic deformation as shown in Eq 8, the true fractured major strain ε_{1f} was evaluated and the fracture strain state was interposed inside FLD.

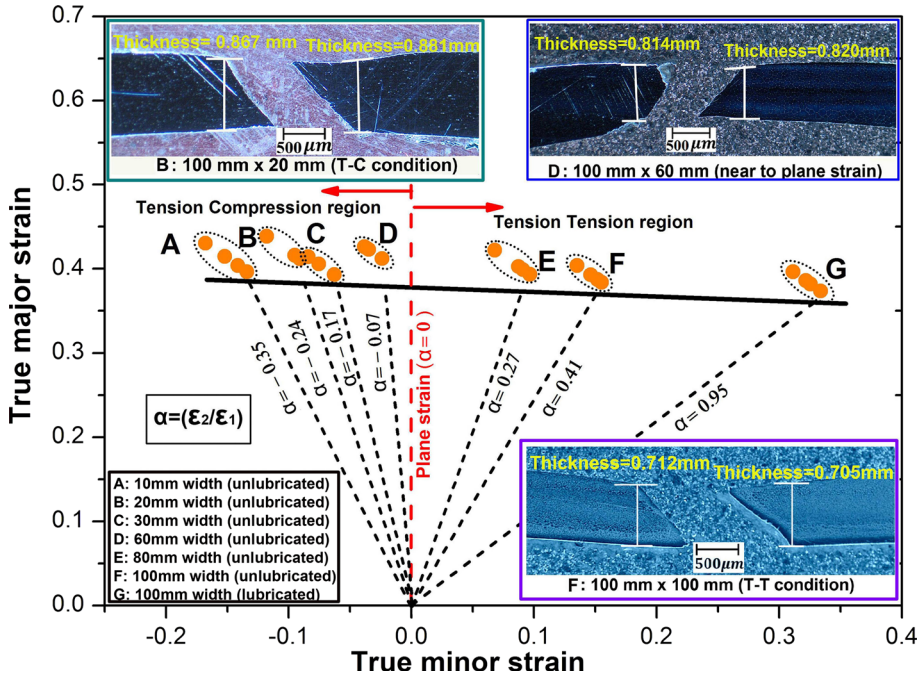

Fig. 12 FFLD diagram showing fractured specimens along thickness direction in T-C, near to plane strain and T-T deformation modes

$$\varepsilon_{1f} + \varepsilon_{2f} + \varepsilon_{3f} = 0 \qquad \text{(Eq 8)}$$

The insets of Fig. 12 depict the thickness measurement of the leaf section in (B) tension-compression (T-C) region, (D) near to plane strain and (F) tension-tension (T-T) region. It was found that the final thickness of the leaf section was gradually decreasing from T-C (0.851 mm) to T-T (0.705 mm) region in the strain ratio ($\alpha = \varepsilon_2/\varepsilon_1$) domain of $-0.35 < \alpha > 0.95$. This decreasing trend in thickness indicated that the material had undergone maximum thinning in tension-tension condition before the onset and further propagation of fracture. The FFLD was drawn as a demarcation of onset of fracture from the major and minor fracture strain data (ε_{1f} and ε_{2f}) obtained from all different LDH specimens, and the same is shown in Fig. 12. The various strain paths (α) are demonstrated in Fig. 12, and the corresponding fractured specimens are shown in Fig. 10.

It was further observed that the shear fracture in T-C and T-T regions has propagated along the thickness direction inclined to the normal surface at an angle approximately 45°. The closeness of FLD and FFLD was further observed at the extreme right-hand side, i.e., the T-T region, as shown in Fig. 12, and this was due to the crack propagation in the thickness direction without any further bulk deformation within the sheet metal. In near to plane strain tensile condition, the fracture propagated through a mixed mode characterized by the onset of localized necking, and the shear fracture propagation took place on further deformation as depicted in the specimen of 100 mm × 60 mm in Fig. 12. It signified that the material had undergone a considerable amount of plastic deformation due to localized straining just before the onset of crack propagation. In the LDH testing, visible necking was also observed while deforming the specimen of 100 mm × 60 mm, and hence, the strain states in FFLD were higher than that in FLD in plane strain condition as shown in Fig. 12.

3.3.3 Effect of Bending on Limiting Strain. As depicted in Fig. 13, the bending strain was induced across the thickness of the sheet due to the use of sub-sized hemispherical punch (ϕ 50 mm) during the LDH test. Hence, the surface strains measured on the deformed specimens were the combination of stretching and bending strains as shown in the top right inset of Fig. 13. The limiting strains of both FLD and FFLD were corrected using Eq 6 and 7. Further, the comparison of the corrected curves considering the bending effect is shown in Fig. 13. It was found that both the corrected FLD and FFLD shifted downward with approximately 4.6 and 3.4% decrease in major strain in plane strain condition. It was observed that the limiting strains in the corrected FFLD were continuously decreasing from T-C region to T-T region, and hence, the fractography studies were carried out to get insight into the failure mechanism during deformation in different strain path in section 3.3.6.

3.3.4 Estimation of Failure Limits in EPS Versus Triaxiality and Stress Space. It was previously reported that the limiting strains represented in major and minor strain space shifted dynamically depending on the type and amount of pre-strain. Hence, this cannot be an effective diagnostic tool to predict failure during deformation along changing strain path. In this context, many researchers had transformed the limiting strains into major (σ_1) and minor stress (σ_2) space (σ-FLDs) and EPS versus triaxiality space ($\bar{\varepsilon}, \eta$) (Ref 33, 58) to restrict the dynamic shift with different pre-strain conditions. Experimentally, the stress values and the triaxiality cannot be determined directly during limiting dome height test, and hence, the Hill-48 plasticity theory was used to transform the experimental strain data of corrected forming and fracture limit diagrams (Ref 59). This anisotropy quadratic yield function (f) can be defined in terms of major (σ_1) and minor (σ_2) stress to estimate effective stress ($\bar{\sigma}$) as in Eq 9.

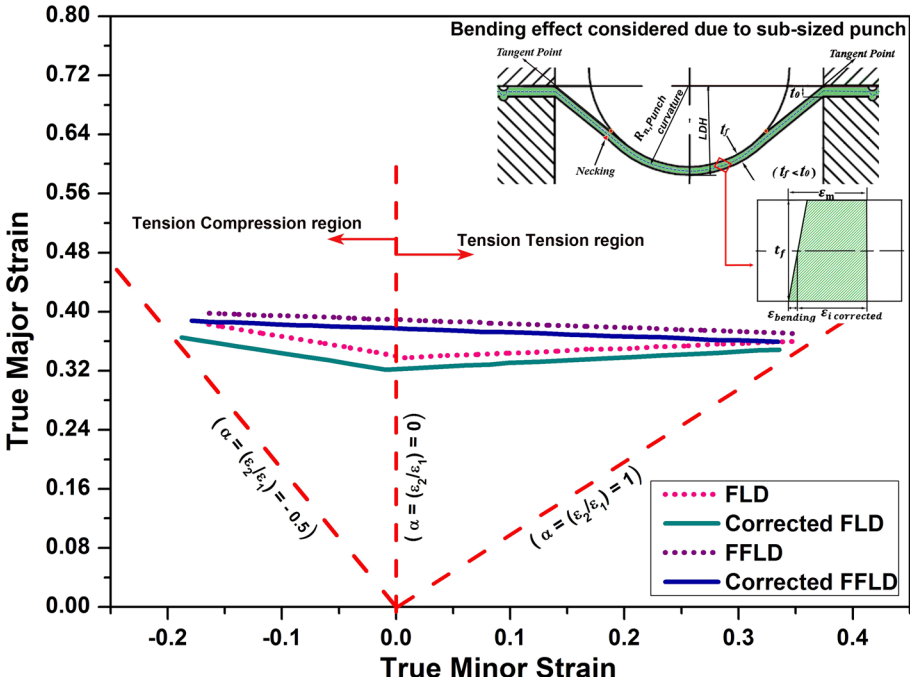

Fig. 13 Measured and corrected forming and fracture limit diagram, and the right top inset demonstrates the effect of bending due to the sub-sized punch

$$f = \sqrt{\sigma_1^2 + \frac{r_0(1+r_{90})}{r_{90}(1+r_0)}\sigma_2^2 - \frac{2r_0}{1+r_0}\sigma_1\sigma_2} = \overline{\sigma} \qquad \text{(Eq 9)}$$

Applying the associate flow rule, $d\bar{\varepsilon}_{ij} = d\lambda \frac{\partial f}{\partial \sigma_{ij}}$ (where $d\lambda$ is a positive scalar that depends on the stress state) in Eq 9, the relation between minor to major strain ratio ($\alpha = \varepsilon_2/\varepsilon_1$) and minor to major principal stress ratio ($\beta = \sigma_2/\sigma_1$) can be established assuming proportional loading during LDH testing as shown in Eq 10.

$$\alpha = \frac{r_0}{r_{90}}\left[\frac{\beta - r_{90}(1-\beta)}{1 + r_0(1-\beta)}\right] \qquad \text{(Eq 10)}$$

From the definition of effective plastic work ($dw = \sigma_1 d\varepsilon_1 + \sigma_2 d\varepsilon_2 + \sigma_3 d\varepsilon_3 = \bar{\sigma} d\bar{\varepsilon}$) and imposing plane stress conditions, the EPS ($\bar{\varepsilon}$) can be expressed as Eq 11.

$$\bar{\varepsilon} = \frac{\left(\varepsilon_1(1+\alpha\beta)\left(\sqrt{r_{90}(1+r_0)}\right)\right)}{\left(\sqrt{r_{90} + r_0\beta^2 + r_0 r_{90}(1-\beta^2)}\right)} \qquad \text{(Eq 11)}$$

From the knowledge of experimental limiting major and minor strain data (from FLD/FFLD), α and β values were calculated. Further, $\bar{\varepsilon}$ was calculated using Eq 11, and $\bar{\sigma}$ was estimated using the hardening law (Eq 2). The major and minor principal stress components were decoupled using Eq 12 and the stress ratio (β). Finally, both the true major and minor stress values were estimated from all the limiting strain data of FLD and FFLD, and these were plotted to generate σ-FLD and σ-FFLD as shown in Fig. 14.

$$\sigma_1 = \frac{\bar{\sigma}}{\left(\sqrt{\frac{r_{90} + r_0\beta^2 + r_0 r_{90}(1-\beta^2)}{r_{90}(1+r_0)}}\right)} \qquad \text{(Eq 12)}$$

In plastic deformation process, the triaxiality (η) can be expressed as the ratio of hydrostatic stress (σ_m) and von Mises stress ($\sigma_{\text{von Mises}}$) components as shown in Eq 13.

$$\eta = \frac{\sigma_m}{\sigma_{\text{von Mises}}} = \frac{(1+\alpha)}{\left(3\sqrt{1+\alpha+\alpha^2}\right)} \qquad \text{(Eq 13)}$$

where $\sigma_m = ((\sigma_1 + \sigma_2)/3)$ for plane stress condition. Equation 11 and 13 were used to estimate $\bar{\varepsilon}$ and η from all the limiting strain data of FLD and FFLD to estimate and plot the ηEPS-FLD and ηEPS-FFLD as shown in Fig. 15. The near-plane strain deformation path with the T-T and T-C regions is also shown both in Fig. 14 and 15. It can be observed that the transformed ηEPS-FFLD is lying above the ηEPS-FLD throughout the deformation path. The triaxiality (η) was found to vary in the range of 0.33 to 0.67 during the LDH test depending on the sample size, and the corresponding stress ratio (β) also varied in the range of 0 to 1. The maximum limit of the triaxiality was obtained during the biaxial stretch forming of 100 mm × 100 mm sample in lubrication condition. Moreover, the EPS was found to increase with triaxiality marginally in T-C region, and thereafter, the curve showed a significant increase toward biaxial tension region. The σ-FLD displays a gradually increasing trend in major limiting stress in the transition from T-C to T-T region. However, σ-FFLD shows an increasing trend up to the plane strain condition and then negligible stress gradient toward biaxial tension region. It was seen that there was a marginal gap between σ-FLD and σ-FFLD in T-C region (3.5% approximately), and this gap increased towards plane strain condition and again decreased towards the biaxial condition. It was noticeable that there was a maximum difference in the limiting strain near to plane strain condition while moving from FLD to FFLD.

3.3.5 FEM Affirmation of Failure Prediction. In order to establish the failure criterion out of the already estimated σ-FLD, σ-FFLD, ηEPS-FLD and ηEPS-FFLD of IN718 material, the FE modeling of the LDH test was done to predict the onset of failure. A one-quarter FE model was developed, where all

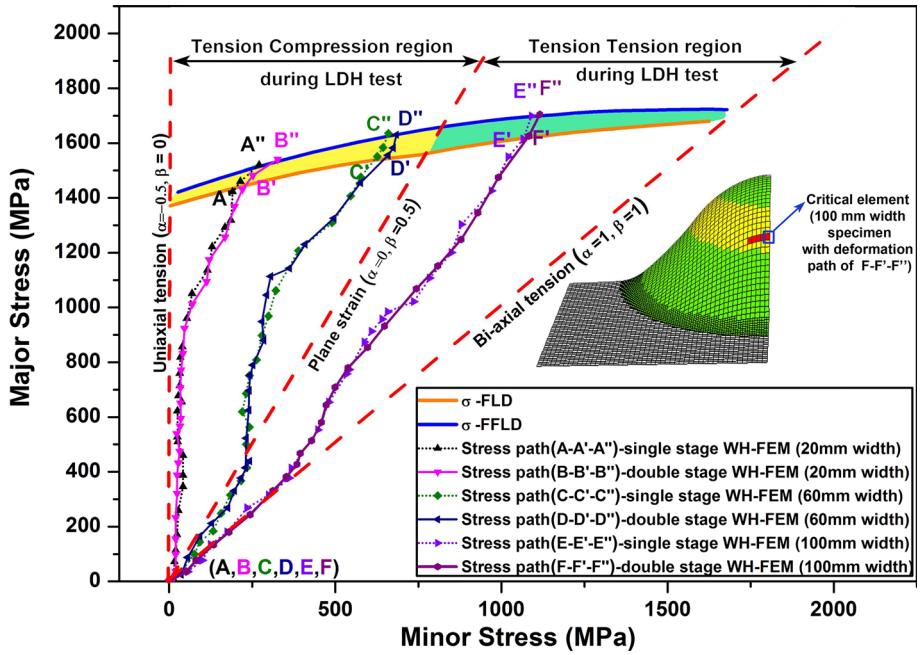

Fig. 14 Stress-based FLD (σ-FLD) and FFLD (σ-FFLD) with deformation path of critical element during single- and double-stage WH behavior, and right inset indicates the critical element which underwent deformation path along $F-F'-F''$

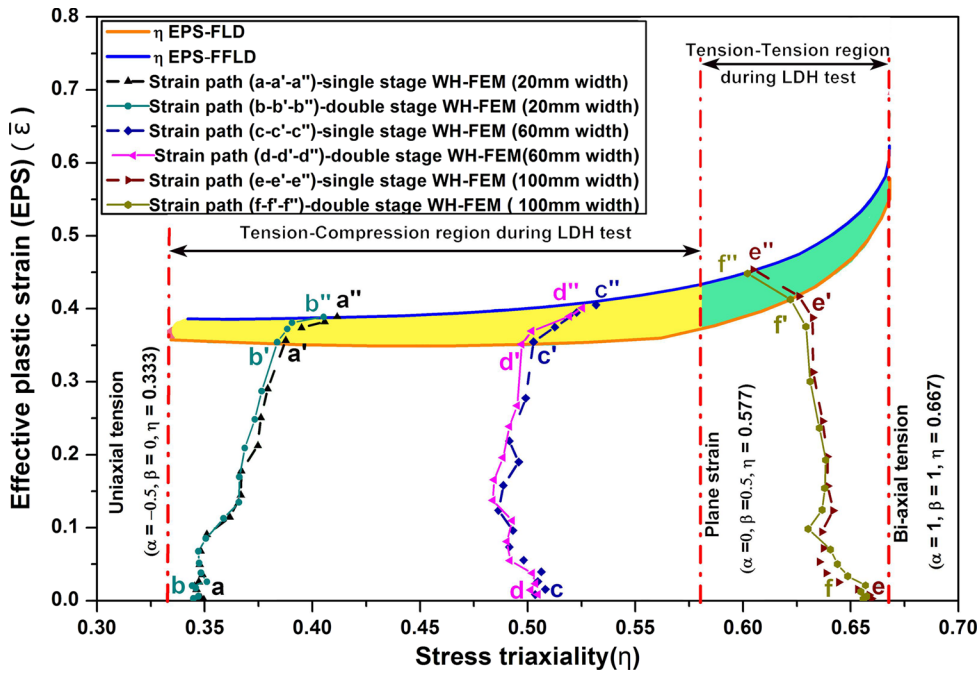

Fig. 15 EPS vs. stress triaxiality plot showing deformation path of the critical element during single- and double-stage WH behavior

the tools such as punch, die and blank holder were assumed as perfectly rigid bodies. The blank was discretized by four-node Belytschko-Tsay shell elements, and the deformation behavior was modeled as per Hill-48 (MAT-122) anisotropy yield criterion (Eq 9). A constant uniform pressure was assigned in the blank holder, and an analytical draw bead was modeled to restrict the material flow from the flange during the stretch forming. The surface-to-surface contact model was adopted using a constant friction coefficient of 0.175 (as obtained from the friction test in Tribometer) as per Coulomb's law of friction.

The numerical simulation was carried out by a commercially available explicit dynamic code, LSDYNA 971. The deformation of the material was modeled using both the single- and double-stage hardening behavior using Swift model to get insight into the change in deformation path. While implementing the double-stage hardening model, both first stage and second stage were incorporated as a single stress-strain curve. The first stage was incorporated (till a plastic strain of 0.075) using the stress-strain response of $1267(\varepsilon_0+\bar{\varepsilon})^{0.2190}$ and second-stage hardening (continued till fracture) using

Table 3 Experimental and FE-predicted LDH comparison

Type of specimen	20 mm width (unlubricated)		60 mm width (unlubricated)		100 mm width (unlubricated)	
Failure limit criteria with hardening stage	σ-FLD or ηEPS-FLD	σ-FFLD or ηEPS-FFLD	σ-FLD or ηEPS-FLD	σ-FFLD or ηEPS-FFLD	σ-FLD or ηEPS-FLD	σ-FFLD or ηEPS-FFLD
FE-predicted LDH (single-stage WH)	21.22	21.98	21.92	23.29	24.17	25.40
FE-predicted LDH (double-stage WH)	21.12	21.87	21.88	23.14	24.04	25. 21
Experimental LDH	21.71 ± 0.15		22.94 ± 0.13		24.86 ± 0.16	

$2088(\varepsilon_0 + \bar{\varepsilon})^{0.4110}$ as shown in Fig. 9(a). The deformation path during the LDH test was estimated from the local stress and strain data of the failure zone from FE simulation, and these were interposed inside the σ-FLD, σ-FFLD, ηEPS-FLD and ηEPS-FFLD to predict the failure step when the limiting strains and stresses were reached.

An identified critical element (Fig. 14) of 100-mm width (unlubricated) specimen implementing double-stage hardening model was considered to plot a deformation path in major-minor stress space ($F - F' - F''$) and effective plastic strain-stress triaxiality space ($f - f' - f''$) as shown in Fig. 14 and 15. The deformation path of three specimens with different widths such as 20, 60 and 100 mm exhibiting single- and double-stage WH behavior is shown in Fig. 14 and 15, and the predicted LDH results are summarized in Table 3. It can be seen from Fig. 14 that the deformation path of the specimen with 20 mm width during the LDH test was along $A - A' - A''$ and it completely lies within the T-C region of the σ-FFLD. The deformation path first intersected σ-FLD at A', and with further deformation, it intersected σ-FFLD at A'. When double-stage hardening model was used, the deformation path changed to $B - B' - B''$, and this led to a minor shift in the intersection points. The corresponding deformation path change in ηEPS window is shown as $a - a' - a''$ and $b - b' - b''$, respectively, in Fig. 15. Similar change in deformation paths for 60-mm (from $C - C' - C''$ to $D - D' - D''$) and 100-mm (from $E - E' - E''$ to $F - F' - F''$) width specimens is shown in Fig. 14. Hence, the predicted LDH results depended on the choice of failure criterion and the selection of hardening model. It was found that the onset of failure step predicted by σ-FLD was the same as that using ηEPS-FLD. Also, the LDH results obtained using the σ-FFLD and ηEPS-FFLD were the same for all the three specimens. The predicted results by σ-FFLD or ηEPS-FFLD were higher, and a minor difference in results was obtained with a change in the hardening model (single stage or double stage). The deformation path of 60-mm specimen was very close to the plane strain deformation mode at the onset of failure, and that of 100-mm width specimen was lying in the T-T region. The use of σ-FFLD or ηEPS-FFLD with the double-stage hardening model predicted the LDH very close to the experimental results.

Further, the FE-predicted major and minor strain distribution of the 100-mm width specimen was compared with those of the experimental data in Fig. 16. It was found that the major strain was positive throughout the curve with the peak at 25 mm away from the pole, and the location of peak coincided with the failure location of the sample as shown in Fig. 17. Further, a well-developed minor strain (Fig. 16b) across the sample indicates tensile-tensile deformation mode, and the strain distribution of IN718 was found to be uniform resulting in far better formability compared to Ti-6Al-4V alloy sheet of similar strength (Ref 44). The major and minor strain profiles were underpredicted by FE model using either σ-FLD or ηEPS-FLD as a failure criterion. At the critical region, the predicted major strain was approximately 12% lower depicting early failure. However, the strain distribution predicted by FE model was matching very well with the experiment date while using the σ-FFLD or ηEPS-FFLD as a failure criterion. The strain path obtained from the single-stage WH overestimated the peak major strain by 5%, and strain distribution profiles predicted by the two-stage WH model were very close to experimental results. The comparison of failure location from FE-predicted

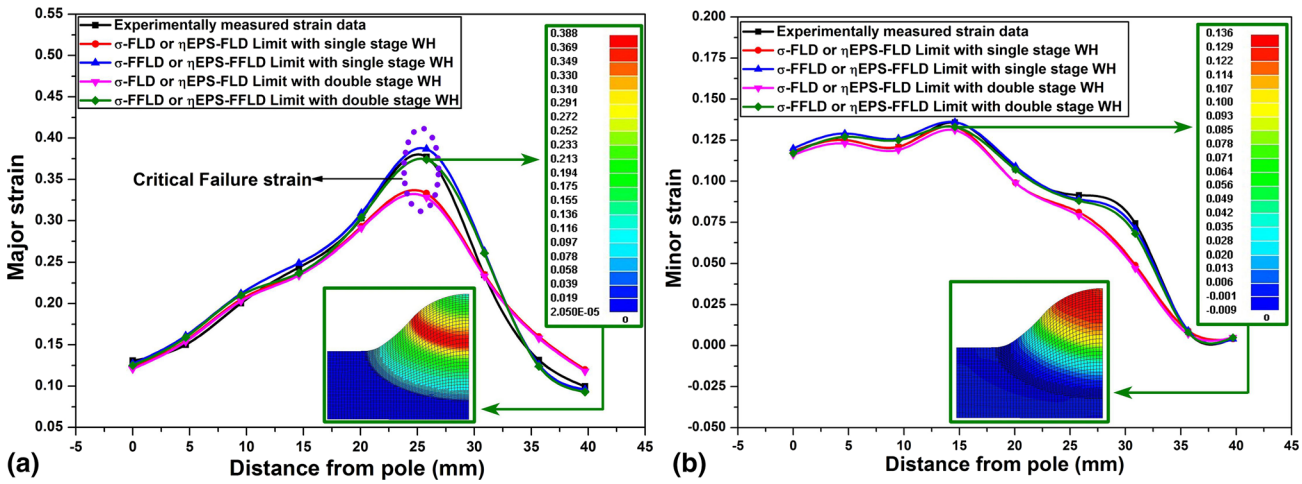

Fig. 16 Comparison of experimentally obtained (a) major and (b) minor strain distribution with FE-predicted strain distribution for 100-mm width specimen

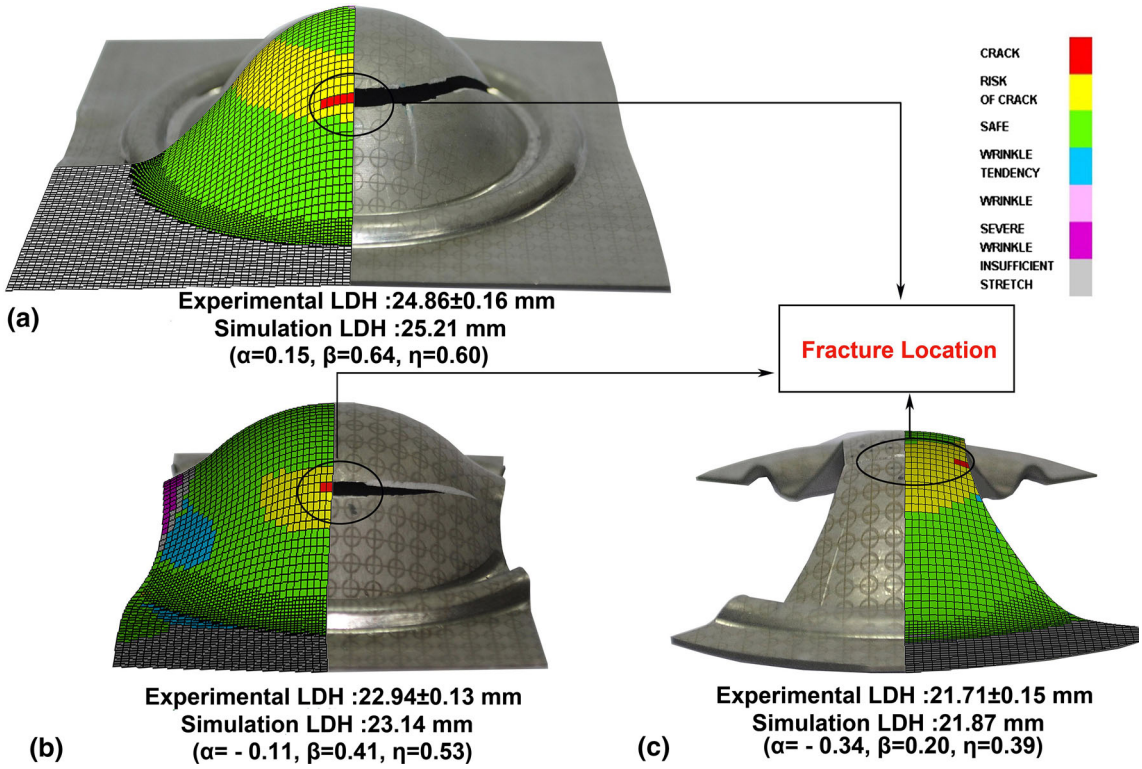

Fig. 17 Experimental and FE-predicted LDH comparison after stretch forming (a) T-T, (b) near to plane strain and (c) T-C condition

results with the experimental observation is shown in Fig. 17. It can be observed that the predicted cup can successfully capture the essential failure features such as failure locations and wrinkling tendency at exact location as compared to experimentally deformed samples. The failure location shifts from the pole depending on the geometry and strain path during deformation which may be due to the difference in strain distribution observed in the component.

3.3.6 Fracture Morphology. The fracture surfaces of the samples deformed in different strain paths (T-C, near to plane strain and T-T) were observed in a scanning electron microscope, and the corresponding fractographs are shown in Fig. 18. The energy-dispersive spectrum (EDS) analysis was carried out to obtain the composition of the inclusion or second-phase particles in the vicinity of the fractured surface. Figure 18(a) shows the fractograph of 20-mm width specimen deformed in tension-compression mode (T-C). Further, the EDS spectrum analysis (Fig. 18b) indicates that the matrix with similar composition as reported in Table 1 is mostly present at the fractured surface. It shows many equiaxed dimples without a trace of any inclusions or second-phase particles within the vicinity of dimples, indicating that the specimen has undergone a large amount of plastic deformation before the onset of fracture due to the ductile rupture of the matrix. This is a clear evidence of higher ductility of the material with larger limiting strains on the left side of FFLD as shown in Fig. 13. The fractograph of the 60-mm width deformed specimen shows shallow dimple structure along with some shear regions as shown in Fig. 18(c), and this indicates characteristics mechanism of quasi-cleavage. Moreover, this specimen had undergone plane strain deformation mode, and the fracture had propagated through carbides as evidence from the EDS results (Fig. 18d). From Fig. 18(e), it can be observed that the fractograph contains predominantly shallow elongated dimple features resulted from the shear-induced failure. Further, a large cluster of spherical carbide particles of <3 μm diameter was found to decorate randomly across and inside the dimple area (Fig. 18f). The presence of a large number of carbides indicated that the crack might have initiated by decoherence of hard-phase particles from the ductile matrix during the biaxial tensile deformation mode. Hence, the fracture limiting strains were lower as observed in FFLD due to high stress concentration at the interface during biaxial tensile deformation mode (T-T mode).

4. Conclusions

The microstructures, forming limit and failure analyses of IN718 sheet materials were studied rigorously in the present work, and it was found that this material showed very high ductility and strength combinations making it suitable for fabrication of Ni-H_2 cell and gas bottle casings. The main conclusions based on the results are summarized below:

1. The microstructures of the mill-annealed IN718 material mainly consisted of grains of size 14 μm with several different precipitates. There were traces of $M_{23}C_6$ precipitates along the grain boundaries, and several MC carbides were also observed in the vicinity of grains. Further δ precipitates of different sizes and shapes were found by SEM and TEM, and these were mostly needle-shaped of approximately 1-3 μm length with a width of 0.3 μm and rectangular shaped of approximate length 650 nm and width of 350 nm. Also, very fine precipitates of spherical γ' of approximately 4 nm diameter and ellipsoidal γ'' of

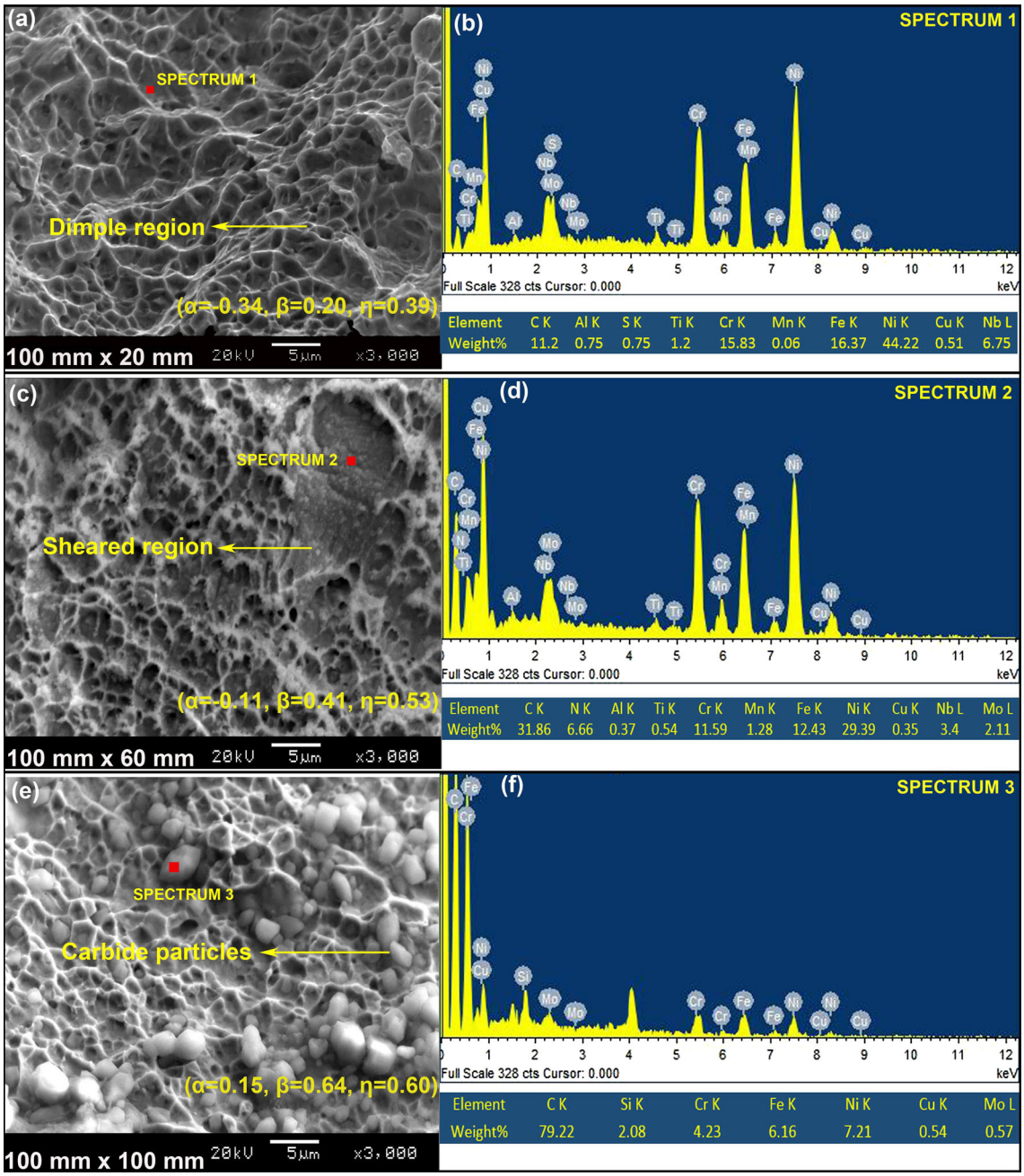

Fig. 18 Fractographs of deformed cups of different geometry (a) 100 mm × 20 mm, (c)100 mm × 60 mm and (e) 100 mm × 100 mm with elemental analysis (b, d, f)

8 nm major diameter with 4 nm minor diameter were present in the IN718 material.

2. The mechanical properties of these rolled sheets were almost similar along different directions with the r values very much close to 1.0. However, the rolled sheet showed high texture with (110) plane normal of most of the grains being parallel to the normal direction of the sheet. This was due to the random distributions of strengthening precipitates in the IN718 material. Moreover, the material showed two stages of work hardening with very high n value due to the accumulation of dislocation bands, dislocation tangling and splitting of dislocation into partial dislocation on interacting with precipitates.
3. The LDH tests were carried out successfully by deforming sheet metals of different width to evaluate the forming limit, and it was found that the IN718 material mostly failed without any prior indication of localized necking. Hence, the fracture forming limit diagram (FFLD) was estimated considering the bending strain induced from the sub-size hemispherical punch of ϕ 50 mm. Approximately 3.4% decrease in major strain was found due to the bending correction in plane strain condition. The failure strains were successfully mapped to estimate strain path-independent σ-FFLD and ηEPS-FFLD of IN718 material for the first time.
4. The σ-FFLD and ηEPS-FFLD with the coefficient of friction evaluated from the Tribometer were implemented in

the FE model, and it was found that the predicted LDH, strain distribution and failure location matched very well with the experimental data. Hence, these calibrated failure limits of IN718 materials can be further utilized as effective tools for designing dies, punches and draw beads, and in selecting process parameters for successful fabrication of aerospace components.

5. Mostly, shear fracture across the thickness was observed at an angle approximately 45° inclined to the normal surface when the IN718 sheets were deformed in both tension-compression and tension-tension mode. Several elongated dimples with the presence of spherical carbide particles indicated decoherence of hard-phase particles from the ductile matrix during the biaxial tension-tension deformation. However, many equiaxed dimples were observed on the fracture surface of tension-compression deformed specimens, and there were no traces of the second phase within the vicinity of dimples. This indicated a large amount of plastic deformation before the onset of fracture due to the ductile rupture of the matrix.

Acknowledgments

Authors wish to express their sincere gratitude to Indian Space Research Organisation (ISRO), Government of India, through Kalpana Chawla Space Technology Cell, IIT Kharagpur (Sanction Number-IIT/KCSTC/CHAIR./NEW.APPR./13-14/64), for providing the financial support.

References

1. H. Yuan and W.C. Liu, Effect of the δ Phase on the Hot Deformation Behavior of Inconel 718, *Mater. Sci. Eng. A*, 2005, **408**, p 281–289
2. H.J. Song, Microstructural Evolution and Deformation Mechanisms in Nickel-Base Superalloys. PhD Thesis, University of Cincinnati, USA, 2010
3. K.S. Prasad, T. Kamal, S.K. Panda, S. Kar, S.V.S. Narayana Murty, and S.C. Sharma, Finite Element Validation of Forming Limit Diagram of IN-718 Sheet Metal, *Mater. Today Proc.*, 2015, **2**(4), p 2037–2045
4. S.C. Krishna, S.K. Singh, S.V.S.N. Murty, G.V. Narayana, A.K. Jha, B. Pant, and K.M. George, Closed Die Hammer Forging of Inconel 718, *J. Metall.*, 2014, **2014**, p 1–7
5. L.H. Thaller and A.H. Zimmerman, Overview of the Design, Development, and Application of Nickel-Hydrogen Batteries, *NASA Tech. Rep.*, 2003, (NASA TP—2003-211905)
6. P. Roamer, C.J. Van Tyne, D.K. Matlock, A.M. Meier, H. Ruble, and F. Suarez, Room Temperature Formability of Alloys 625LCF, 718 and 718SPF, Advanced Steel Processing and Products Research Center Colorado School of Mines Golden, CO 80401, *TMS*, 1997, p 315–329
7. K. Hariharan, N.T. Nguyen, N. Chakraborti, M.G. Lee, and F. Barlat, Multi-objective Genetic Algorithm to Optimize Variable Drawbead Geometry for Tailor Welded Blanks Made of Dissimilar Steels, *Steel Res. Int.*, 2014, **85**, p 1597–1607
8. S.M. Hussaini, G. Krishna, A.K. Gupta, and S.K. Singh, Development of Experimental and Theoretical Forming Limit Diagrams for Warm Forming of Austenitic Stainless Steel 316, *J. Manuf. Process.*, 2015, **18**, p 151–158
9. K. Bandyopadhyay, S.K. Panda, and P. Saha, Optimization of Fiber Laser Welding of DP980 Steels Using RSM to Improve Weld Properties for Formability, *J. Mater. Eng. Perform.*, 2016, **25**, p 2462–2477
10. S.K. Singh, K. Mahesh, A. Kumar, and M. Swathi, Understanding Formability of Extra-Deep Drawing Steel at Elevated Temperature Using Finite Element Simulation, *Mater. Des.*, 2010, **31**, p 4478–4484
11. S.S. Panicker, H.G. Singh, S.K. Panda, and R. Dashwood, Characterization of Tensile Properties, Limiting Strains, and Deep Drawing Behavior of AA5754-H22 Sheet at Elevated Temperature, *J. Mater. Eng. Perform.*, 2015, **24**, p 4267–4282
12. K. Bandyopadhyay, S.K. Panda, and P. Saha, Investigations Into the Influence of Weld Zone on Formability of Fiber Laser-Welded Advanced High Strength Steel, *J. Mater. Eng. Perform.*, 2014, **23**, p 1465–1479
13. K. Hariharan, G. Balachandran, and M.S. Prasad, Application of Cost-Effective Stainless Steel for Automotive Components, *Mater. Manuf. Process.*, 2009, **24**, p 1442–1452
14. R.K. Kesharwani, S.K. Panda, and S.K. Pal, Experimental Investigations on Formability of Aluminum Tailor Friction Stir Welded Blanks in Deep Drawing Process, *J. Mater. Eng. Perform.*, 2015, **24**, p 1038–1049
15. S.P. Keeler, Determination of Forming Limits in Automotive Stampings, *SAE Tech. Pap.*, 1965, **42**, p 683–691
16. G.M. Goodwin, Application of Strain Analysis to Sheet Metal Forming Problems in the Press Shop, *SAE Tech. Pap.*, 1968, **60**, p 764–774
17. S.S. Hecker, Simple Technique for Determining Forming Limit Curves, *Sheet Met. Ind.*, 1975, **52**, p 671–676
18. L.X. Zhou and T.N. Baker, Effects of Strain Rate and Temperature on Deformation Behaviour of IN 718 During High Temperature Deformation, *Mater. Sci. Eng. A*, 1994, **177**, p 1–9
19. X.-M. Chen, Y.C. Lin, D.-X. Wen, J.-L. Zhang, and M. He, Dynamic Recrystallization Behavior of a Typical Nickel-Based Superalloy During Hot Deformation, *Mater. Des.*, 2014, **57**, p 568–577
20. F.-L. Sui, L.-X. Xu, L.-Q. Chen, and X.-H. Liu, Processing Map for Hot Working of Inconel 718 Alloy, *J. Mater. Process. Technol.*, 2011, **211**, p 433–440
21. H.N. Han and K.H. Kim, A Ductile Fracture Criterion in Sheet Metal Forming Process, *J. Mater. Process. Technol.*, 2003, **142**, p 231–238
22. M.B. Silva, M. Skjoedt, A.G. Atkins, N. Bay, and P.A.F. Martins, Single-Point Incremental Forming and Formability–Failure Diagrams, *J. Strain Anal. Eng. Des.*, 2008, **43**, p 15–35
23. K. Isik, M.B. Silva, A.E. Tekkaya, and P.A.F. Martins, Formability Limits by Fracture in Sheet Metal Forming, *J. Mater. Process. Technol.*, 2014, **214**, p 1557–1565
24. A.S. Korhonen and T. Manninen, Forming and Fracture Limits of Austenitic Stainless Steel Sheets, *Mater. Sci. Eng. A*, 2008, **488**, p 157–166
25. M. Gorji, B. Berisha, P. Hora, and F. Barlat, Modeling of Localization and Fracture Phenomena in Strain and Stress Space for Sheet Metal Forming. *Int. J. Mater. Form.*, 2015, **9**, p 1–12
26. J. Jeswiet, F. Micari, G. Hirt, A. Bramley, J. Duflou, and J. Allwood, Asymmetric Single Point Incremental Forming of Sheet Metal, *CIRP Ann. Technol.*, 2005, **54**, p 88–114
27. J.D. Embury and J.L. Duncan, Formability Maps, *Annu. Rev. Mater. Sci.*, 1981, **11**, p 505–521
28. H. Takuda, K. Mori, N. Takakura, and K. Yamaguchi, Finite Element Analysis of Limit Strain in Biaxial Stretching of Sheet Metals Allowing Ductile Fracture, *Int. J. Mech. Sci.*, 2000, **42**, p 785–798
29. M. Jain, J. Allin, and D.J. Lloyd, Fracture Limit Prediction Using Ductile Fracture Criteria for Forming of an Automotive Aluminum Sheet, *Int. J. Mech. Sci.*, 1999, **41**, p 1273–1288
30. S. Basak, S.K. Panda, and Y.N. Zhou, Formability Assessment of Prestrained Automotive Grade Steel Sheets Using Stress Based and Polar Effective Plastic Strain-Forming Limit Diagram, *J. Eng. Mater. Tech.*, 2015, **137**, p 1–12
31. R. Arrieux, C. Bedrin, and M. Boivin, Determination of an Intrinsic Forming Limit Stress Diagram for Isotropic Metal Sheets. In *Proceedings of the 12th Biennial Congress of the IDDRG*, 1982, p 61–71
32. T.B. Stoughton, General Forming Limit Criterion for Sheet Metal Forming, *Int. J. Mech. Sci.*, 2000, **42**, p 1–17
33. T.B. Stoughton and X. Zhu, Review of Theoretical Models of the Strain-Based FLD and Their Relevance to the Stress-Based FLD, *Int. J. Plast.*, 2004, **20**, p 1463–1486
34. Y. Bai and T. Wierzbicki, A New Model of Metal Plasticity and Fracture with Pressure and Lode Dependence, *Int. J. Plast.*, 2008, **24**, p 1071–1096
35. H. Hooputra, G. Metzmacher, and H. Werner, Fracture Criteria for Crashworthiness Simulation of Wrought Aluminum Alloy Components. In *Proceedings of 11th Annual European Conference EuroPam, Heidelberg, Germany*, 2001, p 1–18

36. A.H. Clausen, T. Børvik, O.S. Hopperstad, and A. Benallal, Flow and Fracture Characteristics of Aluminium Alloy AA5083–H116 as Function of Strain Rate, Temperature and Triaxiality, *Mater. Sci. Eng. A*, 2004, **364**, p 260–272
37. AMS 5596 Specification Nickel Alloy, Corrosion and Heat Resistant, Sheet, Strip, Foil, and Plate 52.5Ni 19Cr 3.0Mo 5.1Cb 0.90Ti 0.50Al 18Fe Consumable Electrode or Vacuum Induction Melted, 1775 °F (968 °C) Solution Heat Treated, AMS, *SAE International*, 2012. http://standards.sae.org/ams5596k/
38. M. Xie, Eutectic γ (Ni)/γ′(Ni_3Al)-δ (Ni_3Nb) Polycrystalline Nickel-Base Superalloys: Chemistry, Processing, Microstructure and Properties, *PhD Thesis, Illinois Institute of Technology, USA,* 2012
39. Standard, ASTM, *E8/E8M Standard Test Methods for Tension Testing of Metallic Materials*, ASTM. International, West Conshohocken (PA), 2011
40. J.H. Hollomon, Tensile Deformation, *AIME Trans.*, 1945, **12**, p 1–22
41. H.W. Swift, Plastic Instability Under Plane Stress, *J. Mech. Phys. Solids*, 1952, **1**, p 1–18
42. W.A. Backofen, I.R. Turner, and D.H. Avery, Superplasticity in an Al–Zn Alloy, *Trans. ASM*, 1964, **57**, p 980–990
43. P.L. Charpentier, Influence of Punch Curvature on the Stretching Limits of Sheet Steel, *Metall. Mater. Trans. A*, 1975, **6**, p 1665–1669
44. O.M. Badr, B. Rolfe, P. Hodgson, and M. Weiss, Forming of High Strength Titanium Sheet at Room Temperature, *Mater. Des.*, 2014, **66**, p 618–626
45. J. He, Z.C. Xia, X. Zhu, D. Zeng, and S. Li, Sheet Metal Forming Limits Under Stretch-Bending with Anisotropic Hardening, *Int. J. Mech. Sci.*, 2013, **75**, p 244–256
46. K.S. Prasad, S.K. Panda, S.K. Kar, S.V.S.N. Murty, and S.C. Sharma, Effect of Bending Strain in Forming Limit Strain and Stress of IN-718 Sheet Metal, *Mater. Sci. Forum*, 2015, **830**, p 238–241
47. M.J. Donachie Jr., and O.H. Kriege, Phase Extraction and Analysis in Superalloys-Summary of Investigations by ASTM Committee E-4 Task Group 1, *J. Mater.*, 1972, **7**, p 269–278
48. E.O. Ezugwu, Z.M. Wang, and A.R. Machado, The Machinability of Nickel-Based Alloys: A Review, *J. Mater. Process. Technol.*, 1999, **86**, p 1–16
49. L. Garimella, P.K. Liaw, and D.L. Klarstrom, Fatigue Behavior in Nickel Based Superalloys: A Literature Review, *Jom*, 1997, **49**, p 67–71
50. A. Oradei-Basile and J.F. Radavich, A Current TTT Diagram for Wrought Alloy 718, Superalloys 718, 625 Var. Deriv., *tms.org*, 1991, p 325–335
51. W.C. Liu, F.R. Xiao, M. Yao, Z.L. Chen, Z.Q. Jiang, and S.G. Wang, The Influence of Cold Rolling on the Precipitation of Delta Phase in Inconel 718 Alloy, *Scr. Mater.*, 1997, **37**, p 53–57
52. D.R. Kumar and K. Swaminathan, Formability of Two Aluminium Alloys, *Mater. Sci. Technol.*, 1999, **15**, p 1241–1252
53. S. Iyer, Viscoplastic Model Development to Account for Strength Differential: Application To Aged Inconel 718 at Elevated Temperature, *PhD Thesis, Penn State University, USA,* 2001
54. W.F. Hosford and J.L. Duncan, Sheet Metal Forming: A Review, *Jom*, 1999, **51**, p 39
55. M. Sundararaman, P. Mukhopadhyay, and S. Banerjee, Deformation Behavior of Gamma Double Prime Strengthened Inconel 718, *Acta Met.*, 1988, **36**, p 847–864
56. M. Sundararaman, R. Kishore, and P. Mukhopadhyay, Strain Hardening in Underaged Inconel 718, *Metall. Mater. Trans. A*, 1994, **25**, p 653–656
57. A.G. Atkins, Fracture in Forming, *J. Mater. Process. Technol.*, 1996, **56**, p 609–618
58. G. Maresca, P.P. Milella, and G. Pino, A Critical Review of Triaxiality Based Failure Criteria, *Con. IGF XIII Cassino, 1997*, 2008
59. R. Hill, A Theory of the Yielding and Plastic Flow of Anisotropic Metals, *Proc. R. Soc. London A: Math. Phys. Eng. Sci.*, 1948, **193**, p 281–297